Nanomechanical and Structural Study of Au38 Nanocluster Langmuir-Blodgett Films Using Bimodal Atomic Force Microscopy and X-Ray Reflectivity

Michal Swierczewski, Alexis Chenneviere, Lay-Theng Lee, Plinio Maroni, Thomas Bürgi

To cite this version:

Michal Swierczewski, Alexis Chenneviere, Lay-Theng Lee, Plinio Maroni, Thomas Bürgi. Nanomechanical and Structural Study of Au38 Nanocluster Langmuir-Blodgett Films Using Bimodal Atomic Force Microscopy and X-Ray Reflectivity. Journal of Colloid and Interface Science, In press, ⟨10.1016/j.jcis.2022.10.081⟩. ⟨hal-03830979⟩

HAL Id: hal-03830979
https://hal.science/hal-03830979v1

Submitted on 26 Oct 2022

Nanomechanical and Structural Study of Au_{38} Nanocluster Langmuir-Blodgett Films Using Bimodal Atomic Force Microscopy and X-Ray Reflectivity.

Michal Swierczewski,[a] Alexis Chenneviere,[b] Lay-Theng Lee,*[b] Plinio Maroni*[a] and Thomas Bürgi*[a]

[a] M. Swierczewski, Dr. P. Maroni and Prof. T. Bürgi
Department of Physical Chemistry
University of Geneva
30 Quai Ernest-Ansermet, CH-1211 Geneva 4, Switzerland
Michal.Swierczewski@unige.ch
Plinio.Maroni@unige.ch

[b] Dr. A. Chenneviere and Dr. L.-T. Lee
Laboratoire Léon Brillouin
Université Paris-Saclay
CEA-Saclay, 91191 Gif-sur-Yvette Cedex, France
Alexis.Chenneviere@cea.fr
Lay-Theng.Lee@cea.fr

Corresponding Author: Thomas Bürgi
Phone: +41 22 37 96552
Fax: +41 22 37 96103
E-mail: Thomas.Buergi@unige.ch

Abstract

Hypothesis
Langmuir-Blodgett (LB) technique allows the deposition of gold nanoparticles and nanoclusters (atomically precise nanoparticles below 2 nm in diameter) onto solid substrates with an unprecedented degree of control and high transfer ratios. Nanoclusters are expected to follow the crinkle folding mechanism, which promotes the formation of trilayers of nanoparticles but kinetically disfavors the formation of the fourth layer.

Experiments
LB films of $Au_{38}(SC_2H_4Ph)_{24}$ nanocluster were prepared at a range of surface pressures in the bilayer/trilayer regime and their internal structure was analyzed with X-ray Reflectivity (XRR) and Grazing-Incidence Wide-Angle X-ray Scattering (GIWAXS). Bimodal atomic force microscopy (AFM) imaging was used to quantify the elastic modulus, which can be correlated with the topography at the same point on the surface.

Findings
Nanocluster bilayers and trilayers exhibited the elastic moduli of ca. 1.2 GPa and 0.9 GPa respectively. Films transferred in the 20-25 mN/m surface pressure regime displayed a particular propensity to form highly vertically organized trilayers. Further compression resulted in disorganization of the layers. Crucially, the use of two cantilevers of contrasting stiffness for bimodal AFM measurements has demonstrated a new approach to quantify the mechanical properties of ultrathin films without the use of deconvolution algorithms to remove the substrate contribution.

Key words: gold nanocluster, bimodal atomic force microscopy (AFM), X-ray reflectivity, Langmuir-Blodgett (LB), nanomechanical mapping, Young's modulus

Introduction

Numerous recent advancements in the development of novel functional devices are contingent on manufacturing two-dimensional (2D) ordered assemblies of metal core nanoparticles encapsulated by organic ligand shells.[1-3] It has been shown that many of the desirable properties that distinguish noble metal nanoparticles from bulk materials, such as the localized surface plasmon resonance, are highly dependent on the local dielectric environment and electromagnetic coupling to their neighbors within the 2D array.[4, 5] Consequently, fabrication of macroscopic 2D assemblies of gold clusters, which are atomically precise nanoparticles smaller than 2 nm, presents a noteworthy anticipation in attempts to enhance their interesting electronic,[6] chiroptical[7] and chemical properties[8] through their cumulative behavior. Simultaneously, deposition on substrates is a key requirement enabling the prospective applications of Au clusters in the fields of sensing, catalysis and nanoelectronics.[9, 10]

Particular attention should be devoted to the $Au_{38}(SR)_{24}$ cluster distinguished by its intrinsic chirality, which entails its prominent prospect as a spin-filter device owing to the chiral-induced spin selectivity effect.[11] Despite the relative polydispersity being known to increase for small nanoparticles in this size regime (~1.1 nm core diameter),[12] gold clusters are very highly monodisperse due to the electronic stabilization.[13] Although numerous groups have studied the effect of ligand coverage on the nanoparticles Langmuir films,[14-16] in the case of atomically-precise gold clusters the number of ligands protecting each metal core is constant and enforced by the closed electron-shell and geometrical constraints.[17] Furthermore, this prolate cluster exhibits exceptional stability imperative for efficient molecule ordering, as we have demonstrated by fabricating hexagonally close-packed 2D assemblies of $Au_{38}(SC_2H_4Ph)_{24}$ using Langmuir-Blodgett (LB) technique with subsequent imaging by fast atomic force microscopy (AFM).[18]

Abbreviations: AFM – Atomic Force Microscopy, AM – Amplitude Modulated, AM-FM – Amplitude Modulated-Frequency Modulated, B – bending stiffness, E – Elastic Modulus, GIWAXS – Grazing-Incidence Wide-Angle Scattering, LB – Langmuir Blodgett, Q – momentum transfer, SLD – Scattering Length Density, XRR – X-Ray Reflectivity.

The LB method relies on dispersing a solution containing the desired molecule on top of the air/water interface and, following solvent evaporation, laterally compressing movable barriers while simultaneously monitoring the arising changes in the surface pressure. The deposition onto solid surfaces is achieved by extracting the substrate that had been previously vertically immersed in the water. The main advantages of the LB technique are the high control of the layer based on the surface pressure feedback, as well as the possibility to extend the film over a large area.

A comprehensive understanding of the metal nanoparticle behavior in the Langmuir film and the collapse of the monolayer into bi- and trilayers has been achieved through the use of X-ray reflectivity and related surface specific X-ray techniques.[5, 19-21] Of particular relevance is the study by Dai et. al,[22] where the evolution of the Au nanoparticles film (6 nm diameter) was followed with sub-minute temporal resolution by grazing incidence X-ray off-specular scattering. Two folding mechanisms involving the hypothesized “hash” intermediate phase were discussed: The S-fold and the crinkle fold, with the latter being less kinetically costly. Furthermore, the proposed crinkle fold mechanism demonstrated that although buckling of nanoparticles until three layers of nanoparticles is kinetically facile, pushing up a particle into the fourth layer would involve a movement of multiple particles simultaneously, thus presenting a high kinetic barrier for further multilayer formation. The bending rigidity of Au nanoparticle Langmuir films as well as the monolayer to multilayer transitions have also been studied by Kim et. al.[23] Particularly relevant for our study of gold nanoclusters is their conclusion that unlike films of larger dodecanethiol-capped particles, 2 nm Au nanoparticles films do not form buckling patterns under high compression.

Nonetheless, despite being crucial for the development and the durability of novel functional devices, the nanomechanical properties of ultrathin films of small metal nanoparticles deposited on solid substrates remain unexplored. This is particularly the case for gold nanoclusters whose mechanical properties have never been studied before. Even though they exhibit weak intermolecular forces due to their small size, their exceptional monodispersity allows for enhancement of their fascinating properties through collective action, simultaneously enabling efficient ordering within the 2D array to even further increase their potential.

In this study we combine X-ray based surface techniques with AFM viscoelastic mapping to obtain both structural and nanomechanical information on LB films of racemic $Au_{38}(SC_2H_4Ph)_{24}$ transferred onto silicon substrate in a range of surface pressures 10-30 mN/m. X-ray reflectivity (XRR) probes the vertical composition and structure of the layer while grazing-incidence wide-angle X-ray scattering (GIWAXS) gives information on in-plane organization in the 2D assembly. Bimodal amplitude-modulated frequency-modulated (AM-FM) AFM is used to determine the Young’s modulus of the film that can be correlated directly to its thickness, yielding novel quantitative information on the mechanical properties of these ultrathin films of gold nanoclusters.

Materials and methods

Chemicals: Tetrachloroauric(III) acid trihydrate (HAuCl4·3H2O, 99.99%, Aldrich), 2-phenylethanethiol ($Ph_2C_2H_4SH$, 99%, Aldrich), *L*-glutathione (GSH, 98%, Acros Organics), sodium borohydride ($NaBH_4$, 99.99%, Aldrich), acetone (99.9%, Fisher), tetrabutylammonium hexafluorophosphate ($TBAPF_6$) (98%, Fluka), toluene (99.8%, Fisher), ethanol (99.8% Fisher), methanol (99.9%, Fisher), dichloromethane (HPLC grade, 99%, Carl Roth), *n*-hexane (HPLC grade, 97%, VWR), and chloroform (99.8%, Fisher) were used as received.

Synthesis of $Au_{38}(SC_2H_4Ph)_{24}$: $Au_{38}(SC_2H_4Ph)_{24}$ cluster was prepared according to the previously reported procedure.[17] Briefly, tetrachloroauric acid trihydrate (2.54 mmol) and *L*-glutathione (10.18 mmol) were dissolved in acetone (100 mL) under vigorous stirring for 20 min at room temperature. The yellow suspension was cooled in an ice bath for 20 min. 0.96g of sodium borohydride in 30 mL of pre-cooled Milli-Q water (resistivity 18.2 MΩ cm) was quickly added under vigorous stirring. After 20 min, acetone was decanted and 30 mL of Milli-Q water was added. Ethanol (1.6 mL), toluene (10 mL), and 2-phenylethanethiol (10 mL) were added and the mixture was heated at 80 °C for 24 h. During the long-time etching process, the polydisperse clusters were converted to $Au_{38}(SC_2H_4Ph)_{24}$ clusters. Excess thiol was removed by washing thoroughly with methanol and ethanol. $Au_{38}(SC_2H_4Ph)_{24}$ cluster was extracted from the mixture with toluene. The clusters were purified by passing through a size-exclusion chromatography column packed with Bio-Rad BioBeads SX-1 with toluene used as a mobile phase. The collected fractions were identified by UV-vis spectroscopy with a Varian Cary 50 spectrophotometer using a quartz cuvette of 1 cm path length. Furthermore, matrix-assisted laser desorption/ionization spectra were collected using a Bruker Autoflex mass spectrometer equipped with a nitrogen laser at near threshold laser fluence in positive linear mode. [3-(4-tert-Butylphenyl)-2-methyl-2-propenylidene] malononitrile (DCTB) was used as the matrix with a 1:10, 1:100, and 1:1000 analyte:matrix ratio. A volume of 2 µL of the analyte/matrix mixture was applied to the target and air-dried.

Deposition on silicon using LB Technique: Prior to the deposition, the LB trough (Kibron MicrotroughX) was thoroughly washed with various solvents (acetone, chloroform, ethanol) and filled with Milli-Q water. Typically, 50 µL of solution containing $Au_{38}(SC_2H_4Ph)_{24}$ cluster (1 mg mL^{-1}) dissolved in dichloromethane:*n*-hexane (70:30) was carefully spread on the water surface. After 20 min, the barriers were slowly compressed (1 mm^2 s^{-1}) until the required surface pressure. Vertically immersed Si substrate was retracted upwards with a speed of 1 mm min^{-1}, while the barriers were being compressed to keep the surface pressure constant.

AFM: Standard AC-mode AFM images in air were acquired with an MFP-3D bio Infinity microscope (Asylum Research, Oxford instruments, Santa Barbara, CA). AC240 TS cantilevers (see the specifications below) were used. Cantilevers were excited to free oscillation amplitudes (FOAs) of around 100 nm and the set points were ≈ 80% of the FOAs. The scan rates were typically 0.5-1 Hz. A Cypher AFM (Asylum Research, Oxford instruments, Santa Barbara, CA) was used to perform nanomechanical measurements in air using AM-FM mode (NanoMechPro). Images were acquired with AC160 TS (Asylum Research, Oxford instruments, Taiwan) and AC240 TS (Asylum Research, Oxford instruments, Taiwan) cantilevers, both with nominal tip radius of 7 nm and spring constants of 26 Nm^{-1} and 1.7 Nm^{-1} respectively. Prior to each experiment, cantilever spring constant, resonance frequency, and optical sensitivity were determined using the GetRealTM automatic probe calibration routine included in the AFM software. For quantitative nanomechanical measurements using AC160 TS cantilevers, the FOA of the first mode was kept around 30 nm, the phase around 70 deg and the amplitude of the second mode around 0.3 nm. The free resonant frequencies of the first (f_{01}) and second (f_{02}) mode was 309 kHz and 1.75 MHz respectively. It was ensured that all the AM-FM parameters were kept as similar as possible between the calibration and different samples. The calibration procedure is described in more detail in the SI. Scan rates of around 1 Hz were used. Typically, images of 1000×1000 nm^2 with 256 points and lines were acquired. Gwyddion 2.56[24] and AsylumResearch (version 16.10.211) were used for data visualization and analysis.

XRR: Specular XRR and GIWAXS experiments were performed on a Xeuss 2.0 instrument (Xenocs, France) with a microfocused Cu k-alpha source (wavelength = 1.54 Å) and a Pilatus3 2-D detector (Dectris, Switzerland). The samples were attached to the sample holder and the measurements were carried out in a horizontal configuration with two beam collimation slits (height x width), 0.5 mm × 1.2 mm and 0.3 mm × 1.2 mm, and a sample-detector distance = 1214 mm for XRR. For GIWAXS, the measurements were carried out at near-total reflection configuration with beam collimation slits, 0.6 mm × 0.6 mm and 0.5 mm × 0.5 mm, and a sample-detector distance = 221 mm. In both cases, the sample area probed was of the order of several tens of mm^2. The total acquisition time per sample was about 3 h for XRR and about 15 h for GIWAXS. The reflectivity curves were fitted with an n-layer model with the scattering length density normal to the interface SLD(z) given in Equation 1.

$$SLD(z) = \sum_0^N \left(\frac{SLD_i - SLD_{i+1}}{2}\right)\left(1 - erf\frac{(z - z_i)}{\sigma_i}\right) \qquad (1)$$

where SLD$_i$ and (z_i - z_{i+1}) are the scattering length density and the thickness of layer *i*, respectively, and σ_i is the interfacial roughness between layer *i* and *i*+1 described by an error function. n = 0 (SLD$_0$ = 0) and n = N+1 (SLD$_{N+1}$ = 19.7 × 10^{-6} Å^{-2}) represent the two semi-infinite media, air and silicon substrate, respectively. The best-fit set of parameters was determined by minimization of the χ^2 parameter between the experimental and theoretical curve calculated using the classical optical matrix formalism.[25]

Results and discussion

The isotherms corresponding to the LB compression of $Au_{38}(SC_2H_4Ph)_{24}$ nanocluster and the surface morphology and internal structure of films transferred onto mica in the surface pressure regime below 20 mN/m have been described in our previous study[18] where we focused on the mode of film transfer. In the present study, we examine films compressed to higher pressures transferred onto silicon wafer, in the range 10 – 30 mN/m, where bilayer and trilayer are formed, from very well-organized vertical structure to film collapse and degraded ordering due to over-compression (see Figure S1 for the compression isotherm).

Single mode AFM

The AFM images of surface morphologies of films transferred onto silicon wafer at different pressures are shown in Figure 1. At a surface pressure of 10 mN/m the coverage is significant but far from complete and the average height is around 3-4 nm. Upon increasing the pressure to 20 mN/m, the circular shaped morphology that dominates to minimize the free energy is further brought into contact and the film forms an almost complete layer with a height of 4.5-6 nm. Further area reduction to 30 mN/m leads to the appearance, in some localized regions, of elongated structures perpendicular to the direction of the compression (Fig 1(c)). These structures can reach heights up to 20-30 nm and interestingly, are reminiscent of periodic “wrinkles” reported in the literature for polymeric[26, 27] and nanoparticle[22, 23, 28] thin films on a liquid surface. They result from film instability and collapse due to lateral over-compression, a response that is related to the bending stiffness of the film, $B = (\lambda/2\pi)^4 K$. λ is the periodicity of the wrinkles and $K = \rho g$ the stiffness of the substrate, where ρ is the liquid density and g the gravitational acceleration.[26, 27] The bending stiffness depends on the composition of the film. For our $Au_{38}(SC_2H_4Ph)_{24}$ films, the wrinkle-like features are most likely pre-formed on the water due to over-compression. In this case, assuming that the wrinkle periodicity does not change significantly when the film is transferred onto the solid support, and using the periodicity extracted from Fig 1(c), we obtain $\lambda \approx$ 8 µm and $B \approx$ 6 kT. Therefore, supposing the elongated features to be an analog of wrinkles, the evaluated bending modulus of the water-supported film is very low. Anomalously low bending moduli ($B \approx$ 0.1 kT) have also been found for films of larger Au nanoparticles by other groups.[23, 28] This has been primarily ascribed to spherical nature of the particles, which permits free rotation with respect to one another, leading to unusually low B, while maintaining high elastic modulus of the film. It should be noted that in our films of $Au_{38}(SC_2H_4Ph)_{24}$ clusters these periodic wrinkles have only been found locally and the majority of the film area is similar to films transferred at 20-25 mN/m, i.e. characterized by an almost complete coverage and a thickness of 5-7 nm, although local aggregates are often found (see Figure S2).

X-ray reflectivity and Grazing-Incidence Wide-Angle Scattering

Reflectivity curves of films deposited at 10, 20 and 30 mN/m measured along the axis perpendicular to the transfer direction are shown in Figure 2. The solid lines are best-fit curves with scattering length density (SLD) profiles shown in the inset, where z = ∞ is the bulk silicon substrate and z = 0 is the air/film interface. The maxima in the SLD profiles correspond to electron-rich gold layers and the local minima to electron-poor thiolate ligands. Note that all samples exhibit an interfacial region between the bulk silicon and the transferred film. This interfacial layer is also observed on pure Si wafer (see Figure S3) and is attributed to a hydrated oxidized layer; note that in the presence of a transferred film some ligand molecules are also expected to contribute to this region. This interfacial layer thus revealed will be crucial for AM-FM AFM data interpretation (see corresponding section).

The film transferred at 10 mN/m is characterized by two gold-rich layers of thicknesses 13.6 ± 0.2 Å and 12.8 ± 0.2 Å, which when combined with the intercalating ligands layer gives a thickness of 30.2 ± 0.6 Å, a value that corresponds very well to the lower bound of height seen from AFM (Fig. 1a). It should be noted that this value does not comprise the part of the ligand shell that is integrated in the hydrated oxide layer as mentioned above. Additionally, there is a region of low electron density at the interface with air, which we interpret as an incomplete layer visible in AFM at contact points between circular islands. The buckling mechanism responsible for these features has been described by us in more detail before.[18] This outer layer has a thickness of 13.1 ± 0.2 Å. Thus overall, the bilayer and the adlayer show a total thickness of 43.3 ± 0.8 Å, which corresponds very well with the upper bound of thickness probed by AFM.

The reflectivity curve of the film deposited at 20 mN/m exhibits interference fringes that indicate a well-defined transferred layer. The fitted SLD shows a well-organized internal structure with a trilayer of gold-rich regions intercalated by ligands. This is in concordance with the high propensity of metal nanoparticles films to collapse into two and subsequently three layers observed by multiple groups.[16, 20-23, 28] The three gold-rich layers, from air to silicon, are characterized by thicknesses of 15.6 ± 0.2 Å, 14.1 ± 0.2 Å and 13.1 ± 0.2 Å respectively, giving an overall film thickness of 48.1 ± 1.0 Å after including the intercalating ligand layers that vary from about 2 to 3 Å. This value is also in good agreement with the thickness of 4.5-6 nm measured by AFM (Fig. 1b). From the interference fringes of the reflectivity curve, a model-independent estimate of the total thickness of the surface layer can be derived from $d = 2\pi/\Delta Q$ where ΔQ is the distance between the local minima. In this case, the estimated value is $d \approx$ 59 Å, which clearly includes part of the hydrated oxidized layer. The film transferred at 25 mN/m shows similar remarkably well-organized trilayer structure (see Figure S3). Further compression until a surface pressure of 30 mN/m leads to an increase in overall thickness of the layer. However, the internal organization appears degraded. Although three gold-rich layers can still be distinguished, their intercalations by ligands are less well defined (see Figure 2c). The total fitted thickness of the film is 56.5 ± 1.0 Å, consistent with the height observed in AFM; the model-independent overall thickness (that includes the interfacial hydration layer) from ΔQ yields $d \approx$ 64 Å.

For this sample, therefore, over-compression is reached at 30 mN/m at which point the vertical order in the film is disrupted and localized wrinkle-like features, adlayers and aggregates appear as shown in Figure S2. Indeed, as discussed above, films of gold clusters are ordered and well-defined up to the trilayer regime, but a further compression and introduction of the fourth layer leads to the breaking of that order. This is in concordance with the crinkle mechanism discussed before, which proposes a kinetic barrier for the formation of the fourth layer associated with simultaneous movement of multiple particles.[22] Interestingly, despite a degraded vertical ordering, in-plane organization within the films remains unchanged. Figure 3 shows the GIWAXS results and the corresponding structure peaks. These amorphous peaks are attributed to inter-cluster correlation distances. The clusters are, therefore, organized within the film and the absence of long-range crystallinity is probably a consequence of the prolate shape of the $Au_{38}(SC_2H_4Ph)_{24}$ cluster molecule, as well as the polydispersity of the system. For all the films transferred in the pressure range 10-30 mN/m, GIWAXS shows structure peaks at $Q_{xy} \approx$ 0.38 $Å^{-1}$ which corresponds to in-plane cluster-cluster correlation distance ≈ 16.5 Å.

We thus show that well-organized trilayer films can be obtained at the optimized pressures of 20 – 25 mN/m. Beyond this pressure at 30 mN/m, this internal vertical organization is disrupted by over-compression but without loss of horizontal in-plane ordering. The fitted XRR parameters are given in Table 1.

Amplitude Modulated-Frequency Modulated Bimodal AFM

The phase output associated with mechanical properties of amplitude modulated (AM) AFM has been used by our group in the past to image individual $Au_{38}(SC_2H_4Ph)_{24}$ cluster molecules.[18] However, there are certain limitations of that technique if one is to extract quantifiable information about mechanical properties: the observable associated with the phase output is the loss tangent (tanδ). In physical terms it can be thought of as the degree of damping (such as vibration) of the surface and can be expressed by the equation tanδ = E''/E', where E'' is viscous (loss) modulus and is the ability of the material to dissipate energy and E' is the elastic (storage) modulus and is the measure of elasticity of the material.[29] As such, single mode AM AFM only yields information about the ratio of dissipative to conservative forces, and therefore, individual properties such as the effective Young's modulus (associated with E' given that the tip is much harder than the sample) cannot be quantified. Furthermore, in practice this also means that if the material of study is not rigid, the apparent topography observed from the amplitude output in AM AFM is convoluted by the local deformation induced by the force exerted by the tip on the soft matter.[30, 31]

The above problems can be successfully alleviated with the help of bimodal AM-FM (amplitude modulated – frequency modulated) AFM, whereby two flexural modes of a microcantilever are excited simultaneously. The first, low frequency eigenmode is driven at a high amplitude, whereas the second, high frequency eigenmode is excited at a small amplitude. It follows that the interaction stiffness experienced by the second eigenmode is approximately constant throughout its own oscillation cycle but it gradually changes along the oscillation trajectory of the first eigenmode. Therefore, the change in stiffness of the first mode scales with the square of the indentation depth but the change in stiffness of the second mode scales linearly with the indentation depth, allowing a distinction between E', E'' and tanδ that is not possible in single mode AFM. Additionally, the two eigenmodes have different weight functions used for integrating the stiffness profiles, where the weight function of the second mode increases drastically with the tip approaching the sample.[32] This leads to bimodal AFM being characterized by high nanomechanical sensitivity and spatial resolution, as demonstrated in numerous studies.[31, 33-36]

The higher sensitivity of the second mode is also reflected in the choice of feedback control for each of the modes. Although many configurations exist,[32, 34] AM-FM combines versatility and simplicity of AM used for the first mode, with high signal-to-noise ratio of FM operation applied to the second mode. As such, bimodal AM-FM AFM has revolutionized the field of nanomechanical imaging by offering sensitivity and speed of imaging unmatched by other techniques including force-distance curves[37] or other parametric methods.[38]

Using the Sneddon/Hertz model for a paraboloid tip of radius R, Equations 2 and 3 were derived to relate the experimental observables to the sample deformation δ and the effective Young's modulus E_{eff}:[31]

$$E_{eff} = \frac{4\sqrt{2}}{\sqrt{R}} Q_1 k_1 \left(\frac{k_2 \Delta f_2}{k_1 f_{02}}\right)^2 \frac{A_1^{3/2}}{A_{01}^2 - A_1^2} \tag{2}$$

and

$$\delta = \frac{1}{2Q_1} \frac{k_1 f_{02}}{k_2 \Delta f_2} \left(A_{01}^2 - A_1^2\right)^{1/2} \tag{3}$$

where Q_1 is the quality factor of mode 1, k_i is the spring constant of mode i, f_{02} and Δf_2 are the free resonant frequency and the frequency shift of the second mode, respectively, and A_{01} and A_1 are the free oscillation amplitude and the set-point amplitude of the first mode, respectively. It should be noted that the single observable Δf_2 contains information about the changes in Young's modulus and deformation while all the other parameters remain unchanged throughout the measurement. Hence, a careful calibration is required to ensure the above parameters do not change in contact with different parts of the sample(s).

The Young's modulus of the samples E' can be quantified after calculating R by measuring a sample of known E'. In this case a polystyrene surface with E' ≈ 3GPa was used as a reference.[39] The calibration procedure is described in more detail in SI. Two different cantilevers were used for the bimodal AFM characterization: stiff AC160TS and softer AC240TS.

The mappings of Young's modulus together with the corresponding height trace for $Au_{38}(SC_2H_4Ph)_{24}$ LB films transferred at 10, 20 and 30 mN/m imaged with an AC160TS cantilever are shown in Figure 4(a). The reported Young's modulus values were calculated by drawing a mask that removes the uncovered areas in the height output and applying the same mask to the Young's modulus map before averaging for multiple samples (see Figure S5). From Eqs 1 and 2, the calculated Young's moduli are 1.22 ± 0.09 GPa, 0.91 ± 0.08 GPa and 0.90 ± 0.08 GPa for the films transferred at 10, 20 and 30 mN/m, respectively.

The film transferred at 10 mN/m is considerably harder than those at 20 and 30 mN/m, which can be explained by its thinner, predominantly bilayer-based structure as determined by XRR. Since the dissipation presumably originates from the organic ligand shell, it is understandable that lower thickness leads to lower dissipation, and hence, higher Young's modulus of the film.

Conversely, the films transferred at 20 and 30 mN/m, which are known from XRR to be dominated by trilayers, have a higher contribution of dissipative forces coming from the organic ligands, and therefore, have a comparatively lower Young's modulus. Importantly, the lack of disparity between the Young's moduli between these two films agrees well with the XRR data in that the emergence of a fourth layer (that would likely further decrease the values of E) is not observed at 30 mN/m. Another indirect conclusion that can be drawn is that the disorganization of the layers in the z direction that originates from over-compression, does not significantly affect the mechanical properties.

Typically, the effective Young's modulus obtained from bimodal AFM measurements has a contribution from the substrate surface, which is usually much harder (E = 130-188 GPa for Si).[40] In order to extract the true value of E for the material of interest, deconvolution techniques that require knowledge about the mechanical properties of the surface as well as precise thickness of the film can be applied. Although this method can be used effectively for samples deposited on pure elemental substrates such as Au,[33, 41] it cannot be used for LB films as during the long submersion in water most substrates become hydrated and porous, leading to very different mechanical properties, which in turn depend on the degree of hydration. As evidenced in the XRR section, all samples exhibit a porous layer of hydrated silicon oxide which has a lower electron density, and a lower Young's modulus, than pure Si or SiO_2. Since the mechanical properties of this softer layer are unknown, the deconvolution method cannot be applied.

This issue was solved by using two types of cantilevers with different stiffness (AC160TS is approximately 10 times harder than AC240TS) for the imaging of the same $Au_{38}(SC_2H_4Ph)_{24}$ film transferred at 10 mN/m (see Figure 4(a) and (b) respectively). Comparing the height and Young's modulus outputs of the film imaged with AC160TS cantilever, it can be concluded that the substrate is softer than the sample, which is not typical in bimodal AFM (brighter regions are associated with higher topographic features in the height output and with higher E' in the elasticity output).[33] Conversely, with the softer AC240TS cantilever it is shown that the substrate is harder than the sample. In order to reach the repulsive phase regime that is a requirement for AM-FM measurements,[30] the setpoint when using AC240TS cantilever had to be much lower. In other words, the softer cantilever needed to be pressed much harder against the surface to obtain a significant mechanical response. This, in turn, leads to a considerable increase in the probing depth (as well as an increase of the average Young's modulus to about 6 GPa).

Combining the results from both cantilevers, it can be deduced that in the case of AC240TS cantilever, the oscillation is large enough that pure Si below the hydrated silicon oxide layer contributes to the measurement of the Young's modulus of the sample. This is not the case for the stiffer AC160TS cantilever, which allows efficient nanomechanical characterization at much smaller oscillation amplitudes. The difference in probing depth exhibited by both cantilevers is demonstrated in indentation outputs shown in Figure S6, where the average indentation depth shown by AC160TS and AC240TS cantilevers was 1.1 nm and 2.4 nm respectively. Therefore, it appears that the elastic modulus thus determined gives a good representation of the $Au_{38}(SC_2H_4Ph)_{24}$ film property as it is not artificially increased by the much harder substrate, and hence does not require deconvolution techniques that are not feasible for inhomogeneous substrates. A drawing demonstrating how the stiffness of the cantilever affects the probing depth of the AMFM AFM measurement and why the stiffer cantilever results in E values that are relatively unaffected by the contribution of hard Si substrate is shown in Figure S7.

Although it has been shown that thicker layers are associated with a lower Young's modulus on the global scale (i.e. comparing average E of the entire image in Figure 4(a)), this conclusion is contradicted if one considers the local nanomechanical changes within one image. From Figure 5(a) it can be qualitatively concluded that the parts of the film transferred at 10 mN/m that are higher than their immediate surroundings in the height output (top) are also harder in the Young's modulus map (bottom). The uncovered substrate was excluded from this analysis. On the other hand, the films transferred at 20 and 30 mN/m showed no such dependence of Young's modulus on the height of the film within one image, which has been demonstrated by plotting the Young's modulus of the films shown in Figure 4(a) as a function height percentile as shown in Figure 5(b). This disparity can be explained by the hypothesis that at 10 mN/m the film is in a transient state, whereby the local stress pushes individual molecules closer together, which leads to denser molecule packing (and thus higher E) and results in buckling up of the neighboring molecules. This would be in concordance with the crinkle folding mechanism proposed by Dai et al.[22] However, once the stable configuration of three layers is reached, the film is allowed to relax, as local regions that are considerably harder than their immediate surroundings are no longer discernible at 20 and 30 mN/m. Thus, in the absence of local stress, the global Young's modulus decreases as a result of higher contribution of dissipative forces originating from the ligand shell.

Conclusions

Information on structural and nanomechanical properties of $Au_{38}(SC_2H_4Ph)_{24}$ films is crucial for its implementation in potential applications as the high costs of the nanocluster can be compensated by creating ultrathin films with a large area. It has been shown by X-Ray reflectivity that films of $Au_{38}(SC_2H_4Ph)_{24}$ transferred using Langmuir Blodgett technique have a particular propensity to form trilayers, as even at lower compression the bilayers tend to locally collapse into trilayers. The optimum condition for transfer is identified to be 20-25 mN/m where exceptionally well-organized trilayers are formed. Beyond this pressure range at 30 mN/m, the vertical organization in the film is significantly degraded; rather than building a four-layer (or more) structure, localized wrinkle-like structures and aggregates are formed. This observation is in concordance with the proposed crinkle folding mechanism suggesting that formation of the fourth layer would be disfavored due to a high kinetic cost.[22] The in-plane correlation distance however remains constant for all the films, indicating that cluster-cluster separation is fixed and blocked at all surface pressures by the ligand shell. Finally, bimodal Atomic Force Microscopy has been used to quantify the elastic moduli of the transferred layers, providing novel results on the mechanical properties of these ultrathin gold cluster films. Furthermore, it has been shown that the use of cantilevers with varying spring constants can be applied to remove the contribution of the substrate to the elastic modulus for materials that do not allow a trivial deconvolution due to inhomogeneous mechanical properties.

Acknowledgements

Generous support by the University of Geneva and the Swiss National Science Foundation (grant number CRSII5_173720) is kindly acknowledged.

References

1. Mezour, M. A.; Perepichka, I. I.; Zhu, J.; Lennox, R. B.; Perepichka, D. F., Directing the Assembly of Gold Nanoparticles with Two-Dimensional Molecular Networks. *ACS Nano* **2014,** *8* (3), 2214-2222.
2. Liu, S.; Zhu, T.; Hu, R.; Liu, Z., Evaporation-induced self-assembly of gold nanoparticles into a highly organized two-dimensional array. *Phys. Chem. Chem. Phys.* **2002,** *4* (24), 6059-6062.
3. Taajamaa, L.; Rojas, O. J.; Laine, J.; Yliniemi, K.; Kontturi, E., Protein-assisted 2D assembly of gold nanoparticles on a polysaccharide surface. *Chem. Commun.* **2013,** *49* (13), 1318-1320.
4. Chen, C.-F.; Tzeng, S.-D.; Chen, H.-Y.; Lin, K.-J.; Gwo, S., Tunable Plasmonic Response from Alkanethiolate-Stabilized Gold Nanoparticle Superlattices: Evidence of Near-Field Coupling. *J. Am. Chem. Soc.* **2008,** *130* (3), 824-826.
5. Velleman, L.; Sikdar, D.; Turek, V. A.; Kucernak, A. R.; Roser, S. J.; Kornyshev, A. A.; Edel, J. B., Tuneable 2D self-assembly of plasmonic nanoparticles at liquid|liquid interfaces. *Nanoscale* **2016,** *8* (46), 19229-19241.
6. Wang, L.-M.; Wang, L.-S., Probing the electronic properties and structural evolution of anionic gold clusters in the gas phase. *Nanoscale* **2012,** *4* (14), 4038-4053.
7. Dolamic, I.; Knoppe, S.; Dass, A.; Bürgi, T., First enantioseparation and circular dichroism spectra of Au38 clusters protected by achiral ligands. *Nat. Commun.* **2012,** *3* (1), 798.
8. Kwak, K.; Kumar, S. S.; Pyo, K.; Lee, D., Ionic Liquid of a Gold Nanocluster: A Versatile Matrix for Electrochemical Biosensors. *ACS Nano* **2014,** *8* (1), 671-679.
9. Li, Z.; Xiao, W.; Huang, R.; Shi, Y.; Fang, C.; Chen, Z., A Gold Nanoclusters Film Supported on Polydopamine for Fluorescent Sensing of Free Bilirubin. *Sensors* **2019,** *19* (7), 1726.
10. Homberger, M.; Simon, U., On the application potential of gold nanoparticles in nanoelectronics and biomedicine. *Philos. Trans. R. Soc. A* **2010,** *368* (1915), 1405-53.
11. Ghazaryan, A.; Paltiel, Y.; Lemeshko, M., Analytic Model of Chiral-Induced Spin Selectivity. *J. Phys. Chem. C* **2020,** *124* (21), 11716-11721.
12. Qian, H.; Eckenhoff, W. T.; Zhu, Y.; Pintauer, T.; Jin, R., Total Structure Determination of Thiolate-Protected Au38 Nanoparticles. *J. Am. Chem. Soc.* **2010,** *132* (24), 8280-8281.
13. Ma, Z.; Wang, P.; Xiong, L.; Pei, Y., Thiolate-protected gold nanoclusters: structural prediction and the understandings of electronic stability from first principles simulations. *WIREs Comp. Mol. Sci.* **2017,** *7* (4), e1315.
14. Reik, M.; Calabro, M.; Griesemer, S.; Barry, E.; Bu, W.; Lin, B.; Rice, S. A., The influence of fractional surface coverage on the core–core separation in ordered monolayers of thiol-ligated Au nanoparticles. *Soft Matter* **2019,** *15* (43), 8800-8807.
15. Jiang, Z.; He, J.; Deshmukh, S. A.; Kanjanaboos, P.; Kamath, G.; Wang, Y.; Sankaranarayanan, S. K. R. S.; Wang, J.; Jaeger, H. M.; Lin, X.-M., Subnanometre ligand-shell asymmetry leads to Janus-like nanoparticle membranes. *Nat. Mater.* **2015,** *14* (9), 912-917.
16. Schultz, D. G.; Lin, X.-M.; Li, D.; Gebhardt, J.; Meron, M.; Viccaro, J.; Lin, B., Structure, Wrinkling, and Reversibility of Langmuir Monolayers of Gold Nanoparticles. *J. Phys. Chem. B* **2006,** *110* (48), 24522-24529.
17. Qian, H.; Zhu, Y.; Jin, R., Size-Focusing Synthesis, Optical and Electrochemical Properties of Monodisperse Au38(SC2H4Ph)24 Nanoclusters. *ACS Nano* **2009,** *3* (11), 3795-3803.
18. Swierczewski, M.; Maroni, P.; Chenneviere, A.; Dadras, M. M.; Lee, L.-T.; Bürgi, T., Deposition of Extended Ordered Ultrathin Films of Au38(SC2H4Ph)24 Nanocluster using Langmuir–Blodgett Technique. *Small* **2021,** *17* (27), 2005954.
19. Chen, Y.-T.; Su, H.-S.; Hung, C.-H.; Yang, P.-W.; Hu, Y.; Lin, T.-L.; Lee, M.-T.; Jeng, U. S., X-ray Reflectivity Studies on the Mixed Langmuir–Blodgett Monolayers of Thiol-Capped Gold Nanoparticles, Dipalmitoylphosphatidylcholine, and Sodium Dodecyl Sulfate. *Langmuir* **2017,** *33* (41), 10886-10897.
20. Bera, M.; Sanyal, M.; Sarkar Pal, S.; Daillant, J.; Datta, A.; Kulkarni, G.; Luzet, D.; Konovalov, O., Reversible buckling in monolayer of gold nanoparticles on water surface. *Europhys. Lett.* **2007,** *78*, 56003.
21. Vegso, K.; Siffalovic, P.; Jergel, M.; Weis, M.; Benkovicova, M.; Majkova, E.; Luby, S.; Kocsis, T.; Capek, I., Silver Nanoparticle Monolayer-to-Bilayer Transition at the Air/Water Interface as Studied by the GISAXS Technique: Application of a New Paracrystal Model. *Langmuir* **2012,** *28* (25), 9395-9404.
22. Dai, Y.; Lin, B.; Meron, M.; Kim, K.; Leahy, B.; Witten, T. A.; Shpyrko, O. G., Synchrotron X-ray Studies of Rapidly Evolving Morphology of Self-Assembled Nanoparticle Films under Lateral Compression. *Langmuir* **2013,** *29* (46), 14050-14056.
23. Kim, K.; Leahy, B.; Dai, Y.; Shpyrko, O.; Soltau, J.; Pelton, M.; Meron, M.; Lin, B., Governing factors in stress response of nanoparticle films on water surface. *J. Appl. Phys.* **2011,** *110*.

24. Nečas, D.; Klapetek, P., Gwyddion: an open-source software for SPM data analysis. *Open Phys.* **2012,** *10* (1), 181-188.

25. M. Born, E. W., *Principles of Optics: Electromagnetic Theory of Propagation, Interference and Diffraction of Light*. Cambridge University Press: Cambridge, 1975.

26. Vella, D.; Aussillous, P.; Mahadevan, L., Elasticity of an interfacial particle raft. *Europhys. Lett.* **2004,** *68* (2), 212-218.

27. Pocivavsek, L.; Dellsy, R.; Kern-Goldberger, A.; Johnson, S.; Lin, B.; Lee, K. Y.; Cerda, E., Stress and Fold Localization in Thin Elastic Membranes. *Science* **2008,** *320*, 912-6.

28. Leahy, B. D.; Pocivavsek, L.; Meron, M.; Lam, K. L.; Salas, D.; Viccaro, P. J.; Lee, K. Y. C.; Lin, B., Geometric Stability and Elastic Response of a Supported Nanoparticle Film. *Phys. Rev. Lett.* **2010,** *105* (5), 058301.

29. Wu, B.; Pu, P.; Zhao, S.; Izadikhah, I.; Shi, H.; Liu, M.; Lu, R.; Yan, B.; Ma, S.; Markert, B., Frequency-related viscoelastic properties of the human incisor periodontal ligament under dynamic compressive loading. *PLoS One* **2020,** *15* (7), e0235822.

30. Benaglia, S.; Amo, C. A.; Garcia, R., Fast, quantitative and high resolution mapping of viscoelastic properties with bimodal AFM. *Nanoscale* **2019,** *11* (32), 15289-15297.

31. Benaglia, S.; Gisbert, V. G.; Perrino, A. P.; Amo, C. A.; Garcia, R., Fast and high-resolution mapping of elastic properties of biomolecules and polymers with bimodal AFM. *Nat. Protoc.* **2018,** *13* (12), 2890-2907.

32. Labuda, A.; Kocuń, M.; Meinhold, W.; Walters, D.; Proksch, R., Generalized Hertz model for bimodal nanomechanical mapping. *Beilstein J. Nanotechnol.* **2016,** *7*, 970-982.

33. Athanasopoulou, E.-N.; Nianias, N.; Ong, Q. K.; Stellacci, F., Bimodal atomic force microscopy for the characterization of thiolated self-assembled monolayers. *Nanoscale* **2018,** *10* (48), 23027-23036.

34. Kawai, S.; Glatzel, T.; Koch, S.; Such, B.; Baratoff, A.; Meyer, E., Ultrasensitive detection of lateral atomic-scale interactions on graphite (0001) via bimodal dynamic force measurements. *Phys. Rev. B* **2010,** *81* (8), 085420.

35. Martinez-Martin, D.; Herruzo, E. T.; Dietz, C.; Gomez-Herrero, J.; Garcia, R., Noninvasive Protein Structural Flexibility Mapping by Bimodal Dynamic Force Microscopy. *Phys. Rev. Lett.* **2011,** *106* (19), 198101.

36. Martínez, N. F.; Lozano, J. R.; Herruzo, E. T.; Garcia, F.; Richter, C.; Sulzbach, T.; Garcia, R., Bimodal atomic force microscopy imaging of isolated antibodies in air and liquids. *Nanotechnology* **2008,** *19* (38), 384011.

37. Heinz, W. F.; Hoh, J. H., Spatially resolved force spectroscopy of biological surfaces using the atomic force microscope. *Trends Biotechnol.* **1999,** *17* (4), 143-150.

38. Rabe, U.; Arnold, W., Acoustic microscopy by atomic force microscopy. *Appl. Phys. Lett.* **1994,** *64* (12), 1493-1495.

39. Moskalyuk, O. A.; Belashov, A. V.; Beltukov, Y. M.; Ivan’kova, E. M.; Popova, E. N.; Semenova, I. V.; Yelokhovsky, V. Y.; Yudin, V. E., Polystyrene-Based Nanocomposites with Different Fillers: Fabrication and Mechanical Properties. *Polymers* **2020,** *12* (11), 2457.

40. Hopcroft, M. A.; Nix, W. D.; Kenny, T. W., What is the Young's Modulus of Silicon? *J. Microelectromech. Syst.* **2010,** *19*, 229-238.

41. DelRio, F. W.; Jaye, C.; Fischer, D. A.; Cook, R. F., Elastic and adhesive properties of alkanethiol self-assembled monolayers on gold. *Appl. Phys. Lett.* **2009,** *94* (13), 131909.

Single column:

Sample	**Layer n**	**SLD (10^{-6} Å^{-2})**	**Thickness (Å)**	**Roughness (Å)**
10 mN/m	0	0		
	1	9.58	13.1	2.4
	2	**18.70**	**13.6**	0.5
	3	6.66	3.8	0.5
	4	**17.90**	**12.8**	0.5
	5	*13.74*	*15.7*	0.5
	N	19.70		4.5
20 mN/m	0	0		
	1	**21.46**	**15.6**	3.8
	2	13.34	3.2	0.5
	3	**23.44**	**14.1**	0.5
	4	13.56	2.1	0.5
	5	**23.74**	**13.1**	0.5
	6	*17.08*	*22.4*	0.5
	N	19.70		1.3
25 mN/m	0	0		
	1	**21.34**	**13.4**	2.8
	2	11.50	3.1	0.5
	3	**23.66**	**13.0**	0.5
	4	15.90	2.2	0.5
	5	**23.36**	**12.1**	0.5
	6	*16.27*	*21.8*	0.5
	N	19.70		4.5
30 mN/m	0	0	**12.1**	
	1	**19.16**	4.4	2.2
	2	15.76	**16.9**	0.5
	3	**21.10**	1.0	0.5
	4	17.26	**12.6**	0.5
	5	**22.70**	**9.0**	0.5
	6	**20.72**	*20.1*	0.5

	7	*15.90*		0.5
	N	19.70		4.9
Pure Si	0	0		
	1	*11.26*	*11.5*	2.9
	2	*18.42*	*10.0*	2.5
	N	19.70	0	3.3

Table 1. Fitted XRR parameters of films of $Au_{38}(SC_2H_4Ph)_{24}$ transferred onto Si in 10-30 mN/m range as well as that of pure Si substrate. Layer 0 and N refer to air and Si substrate respectively. Au-rich layers are labelled in bold. Hydration layers are labelled in italics.

2 columns:

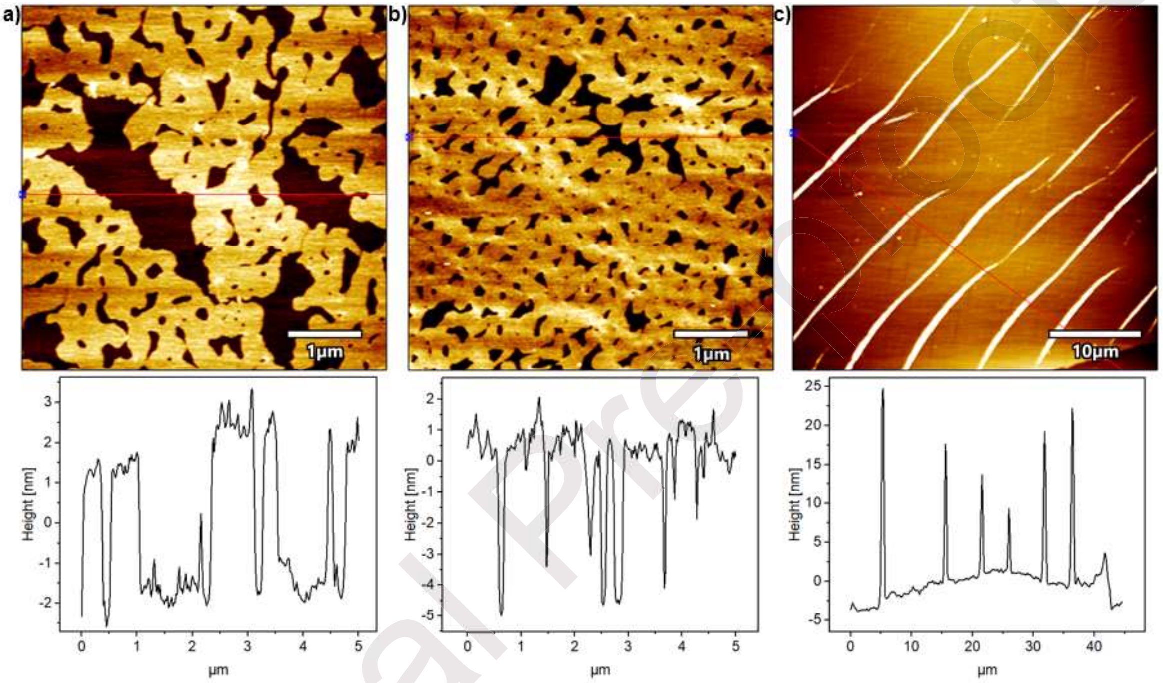

Figure 1. AFM images of LB films of $Au_{38}(SC_2H_4Ph)_{24}$ transferred onto silicon wafer at a surface pressure of (a) 10 mN/m; (b) 20 mN/m and (c) 30 mN/m. The corresponding z -profiles along the red line are shown below.

Single column:

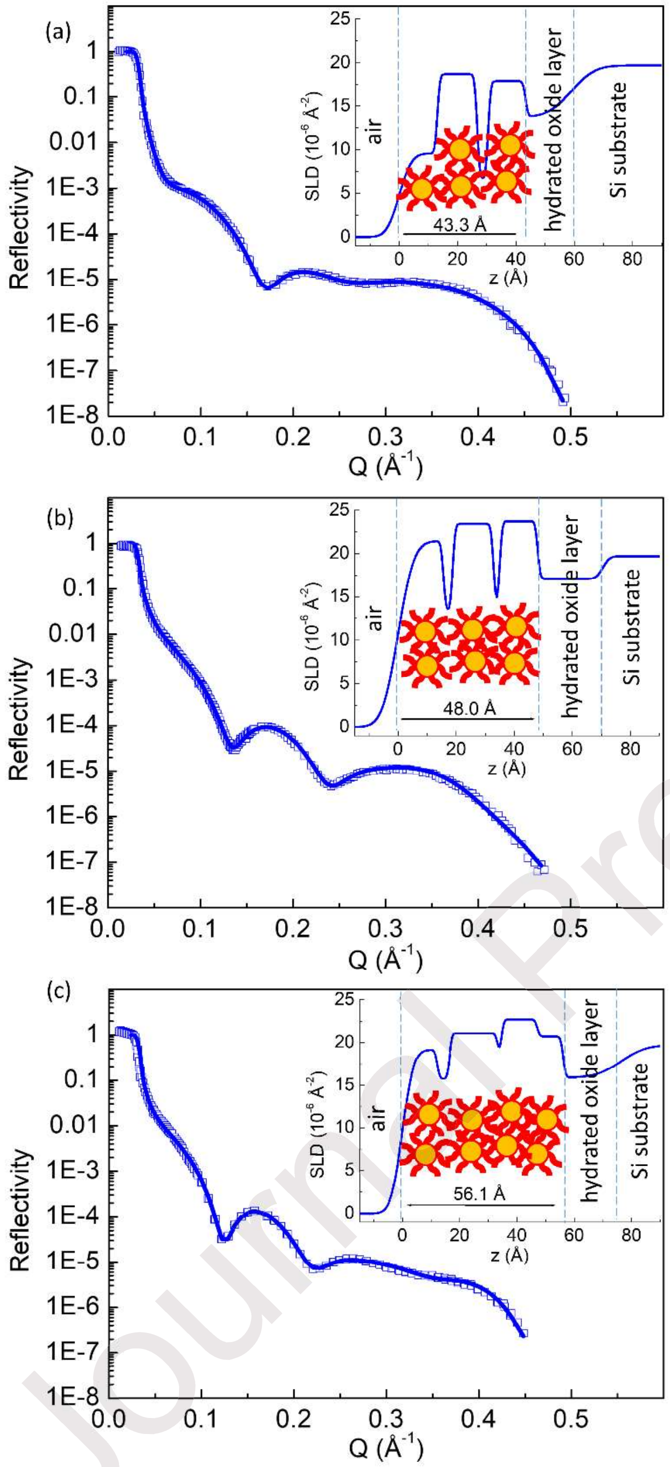

Figure 2. XRR curves of LB films of $Au_{38}(SC_2H_4Ph)_{24}$ transferred at the surface pressure of (a) 10 mN/m; (b) 20 mN/m and (c) 30 mN/m. The solid lines are fitted curves with corresponding SLD profiles shown in the inset.

2 columns:

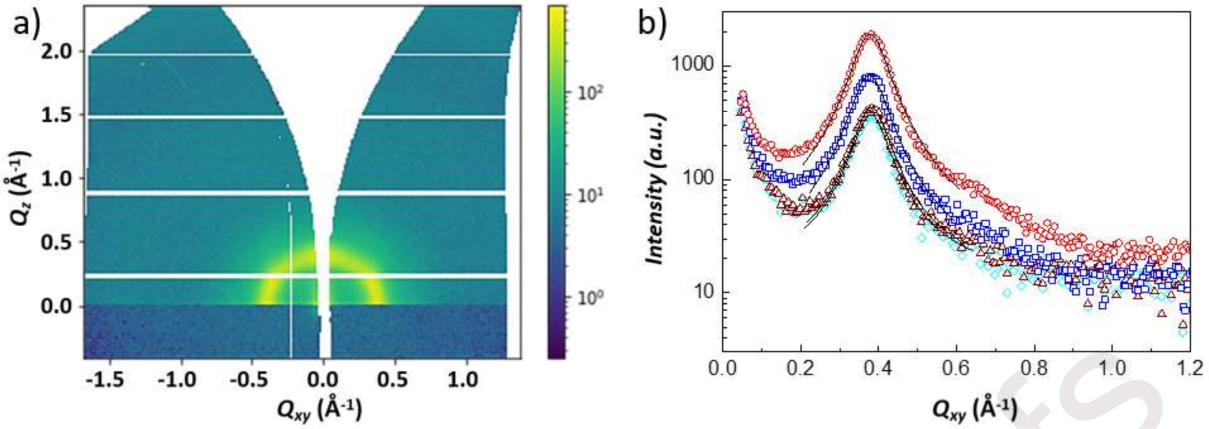

Figure 3. (a) GIWAXS of $Au_{38}(SC_2H_4Ph)_{24}$ film transferred onto Si at 10 mN/m; b) line intensity cut near the Yoneda peak at Qz≈ 0.025 Å^{-1} for films transferred at 10 (cyan), 15 (brown), 20 (blue) and 30 mN/m (red). The remaining GIWAXS plots are included in Figure S4. The solid lines are Lorentzian fits to the correlation peaks at ≈ 0.38 Å^{-1} that correspond to correlation distances of 16.5 - 16.7 Å.

2 columns:

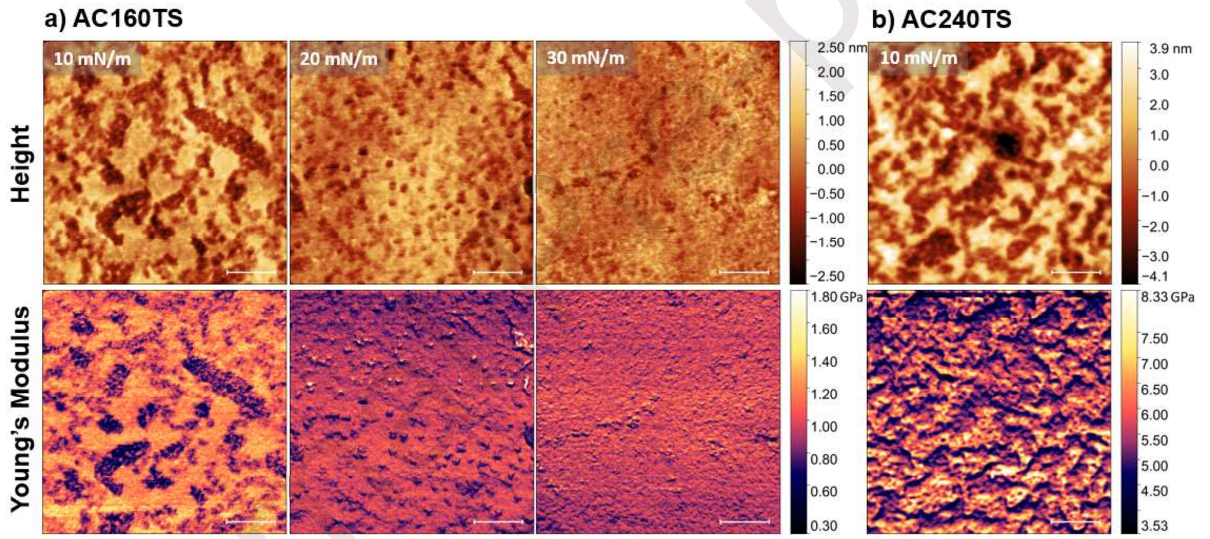

Figure 4. Height outputs (top) and the corresponding Young's modulus outputs (bottom) of films of $Au_{38}(SC_2H_4Ph)_{24}$ transferred onto Si at surface pressures of 10, 20 and 30 mN/m respectively measured by AM-FM AFM using (a) a stiff AC160TS cantilever and (b) a softer AC240TS cantilever. The scale bar corresponds to 200 nm.

Single column:

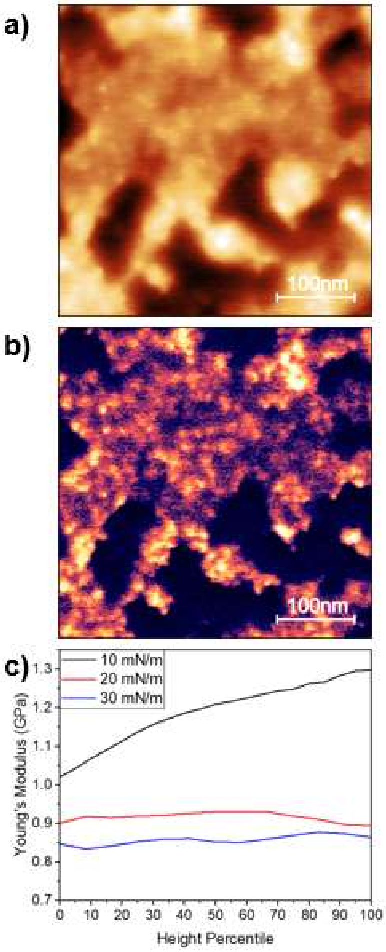

Figure 5. Local changes in Young’s modulus based on a height output (a) and the corresponding Young’s modulus output (b) of a $Au_{38}(SC_2H_4Ph)_{24}$ film transferred onto Si at a surface pressure of 10 mN/m; (c) Plot of changing Young’s modulus at different height percentiles of the films shown in Fig. 4(a).

Supporting Information

Nanomechanical and Structural Study of Au_{38} Nanocluster Langmuir-Blodgett Films Using Bimodal Atomic Force Microscopy and X-Ray Reflectivity.

Michal Swierczewski,[a] Alexis Chenneviere,[b] Lay-Theng Lee,*[b] Plinio Maroni*[a] and Thomas Bürgi*[a]

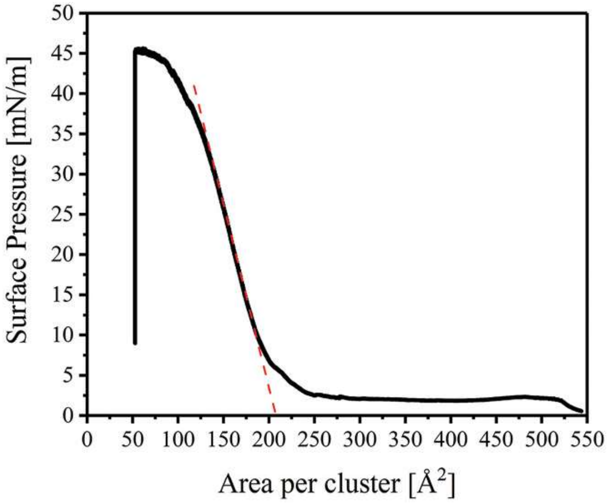

Figure S1. Surface pressure/area isotherm of $Au_{38}(SC_2H_4Ph)_{24}$ film. Dashed line determines the limiting critical area of the molecule at ≈205 Å^2. Reprinted with permission from *Small* **2021**, 17 (27), 2005954.

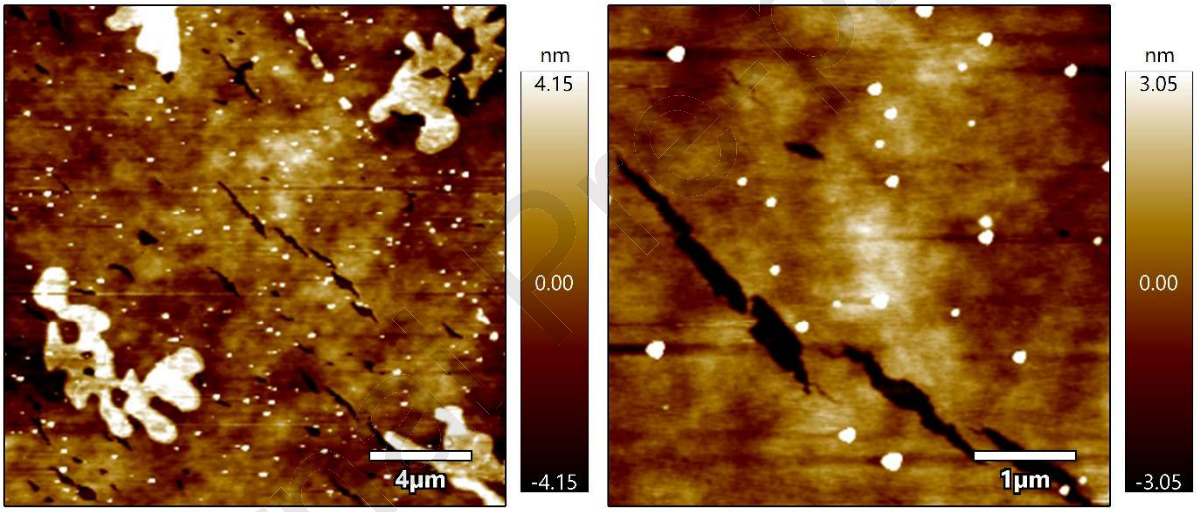

Figure S2. Atomic Force Microscopy (AFM) images of $Au_{38}(SC_2H_4Ph)_{24}$ films transferred at 30 mN/m.

An area far from the periodic wrinkles discussed in the main manuscript is shown. Although almost the entire area is covered by a 5-7 nm thick layer of Au clusters, many aggregates and adlayers are observed.

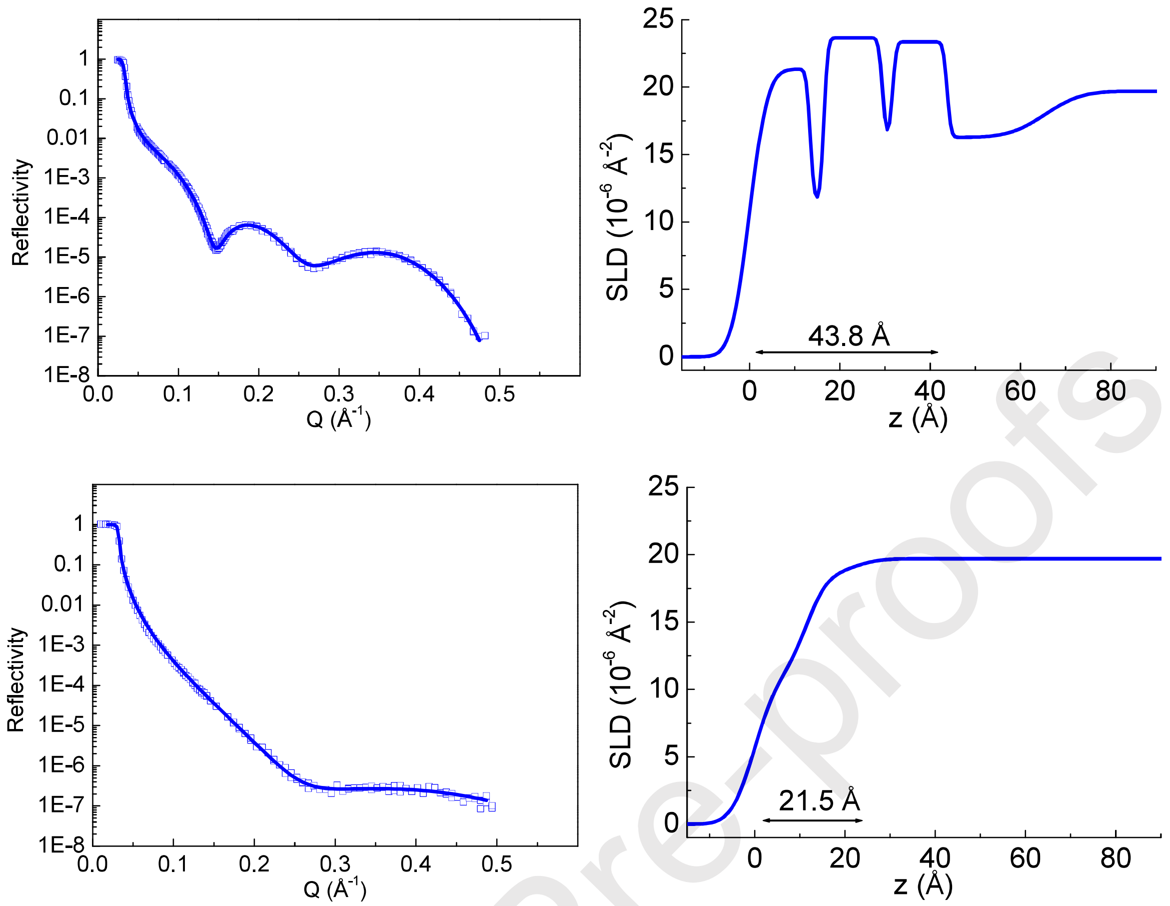

Figure S3. X-Ray Reflectivity (XRR) spectra of $Au_{38}(C_2H_4Ph)_{24}$ film with the corresponding SLD plots transferred onto Si at 25 mN/m (top) and that of pure Si (bottom) referred to in the main manuscript.

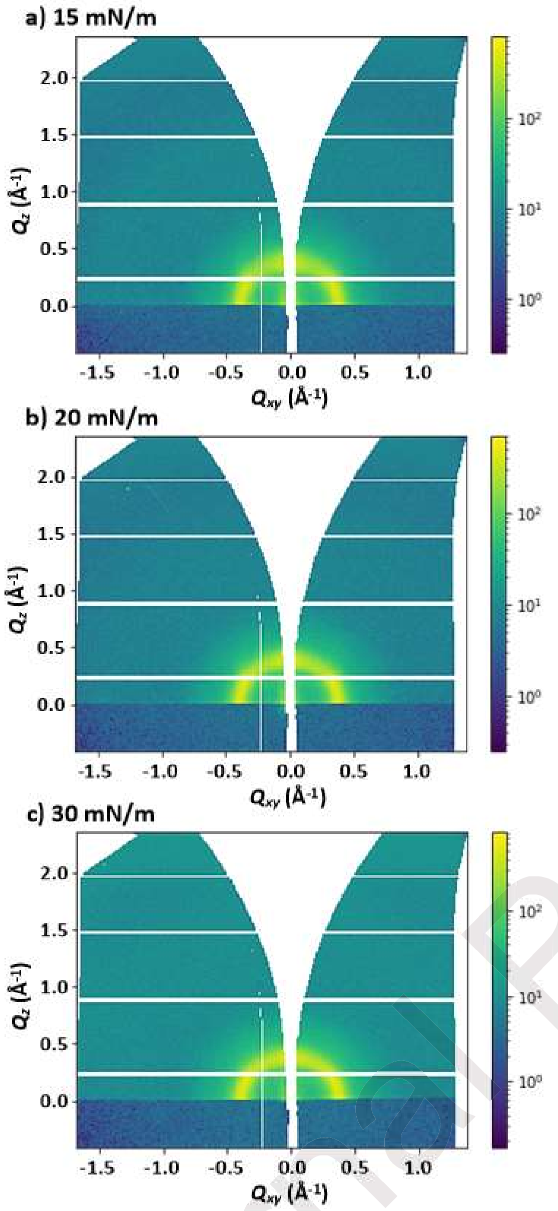

Figure S4. Grazing-Incidence Wide-Angle X-ray Scattering (GIWAXS) spectra of films of $Au_{38}(SC_2H_4Ph)_{24}$ transferred at 15 mN/m (top), 20 mN/m (middle) and 30 mN/m (bottom) discussed in the main manuscript.

The line intensity cut near the Yoneda peak at $Q_z \approx 0.025$ Å^{-1} of the GIWAXS spectra presented here are plotted together in Figure 3(b) of the main manuscript.

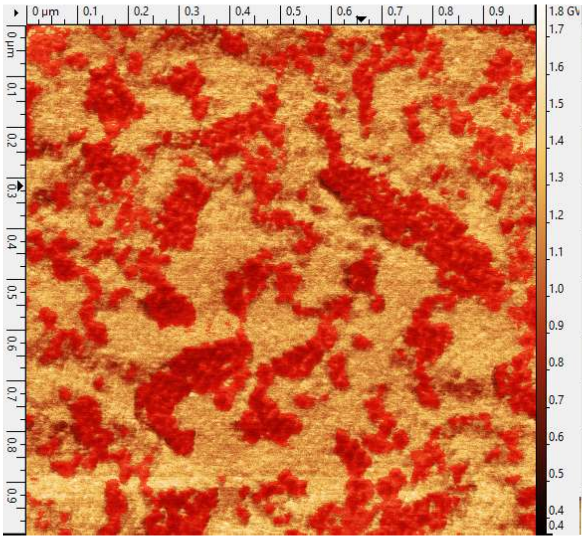

E = 1.16 GPa

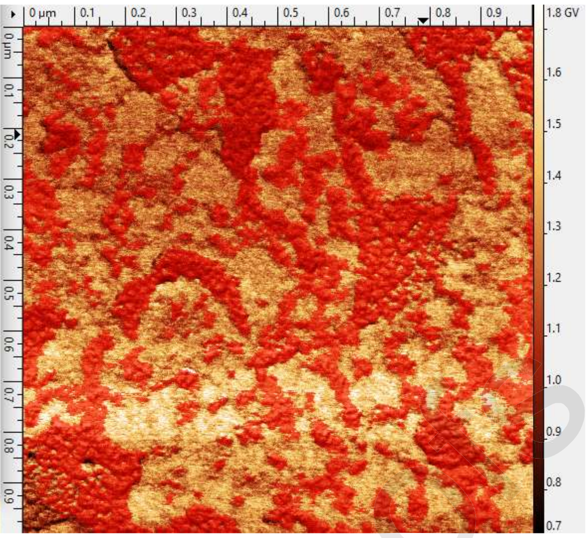

E = 1.276 GPa

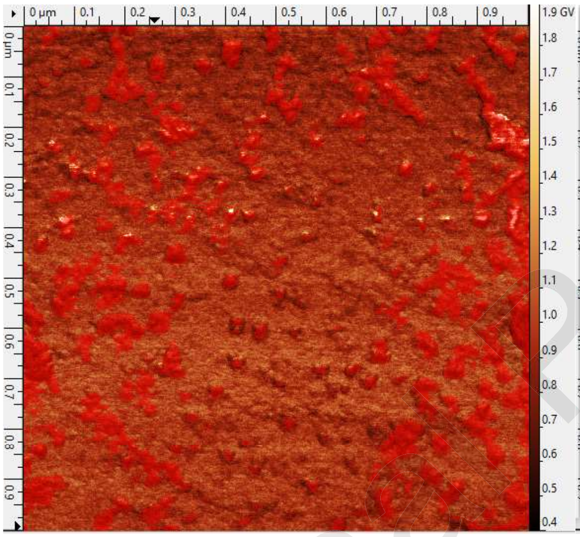

E = 0.940 GPa

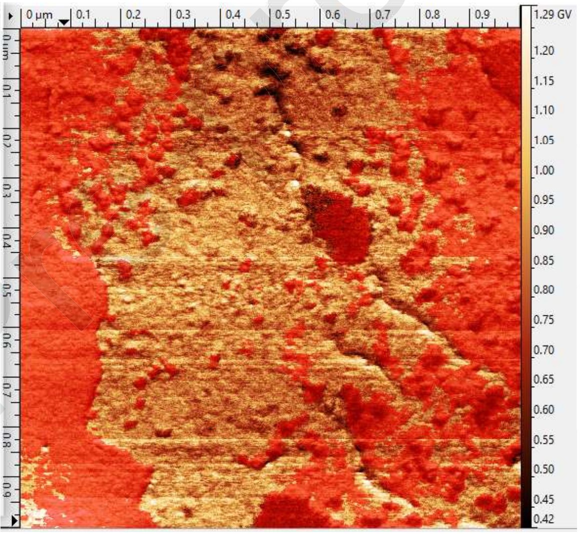

E = 0.871 GPa

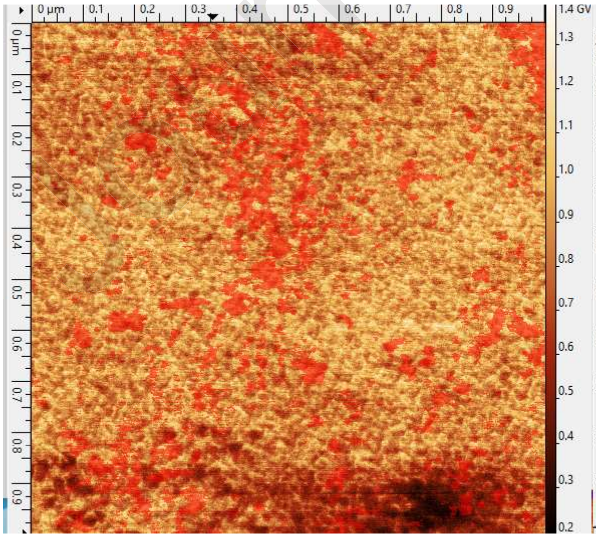

E = 0.857 GPa

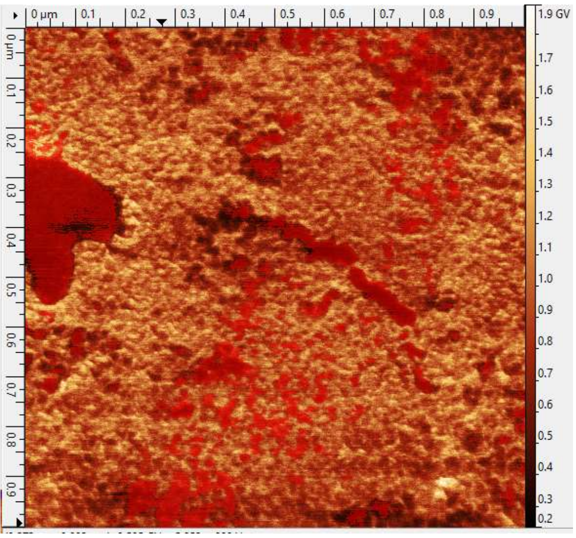

E = 0.933 GPa

Figure S5. Masked area of AM-FM images used for quantifying the elastic modulus E of $Au_{38}(SC_2H_4Ph)_{24}$ films transferred at 10 mN/m (top), 20 mN/m (middle) and 30 mN/m (bottom).

AM-FM elasticity output (following the calibration) measured using the AC160TS cantilever. The mask (shown in red) that excludes the bare substrate was used for calculation included in the main manuscript. The value given in the main manuscript is an average of the two images considered here. It should be noted that it was crucial that the shape of the tip does not get changed during the measurement in order to quantify the Young's modulus accurately (see calibration section below for more detail). This is the reason why only two images of each sample were used for the calculation of E.

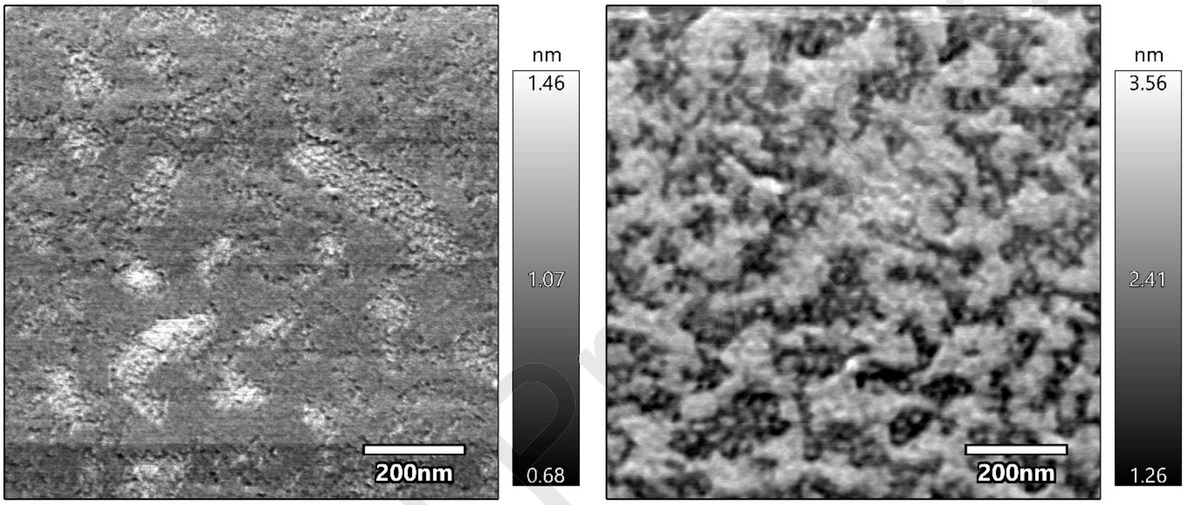

Figure S6. Indentation output of $Au_{38}(SC_2H_4Ph)_{24}$ LB film transferred at 10 mN/m measured with AC160TS (left) and AC240TS (right) cantilever demonstrating the average indentation depth of 1.1 nm and 2.4 nm respectively.

AC160TS
Stiff cantilever → low amplitude required to reach a good nanomechanical response → negligible contribution from hard Si → relatively unaffected E values for the LB film

AC240TS
Soft cantilever → high amplitude required to reach a good nanomechanical response → high contribution from hard Si → inflated E values for the LB film

Figure S7. A drawing aiming to demonstrate why the two cantilevers with different stiffness have a different probing depth in AM-FM AFM measurements.

AM-FM cantilever calibration

In order to get quantitative nanomechanical information, the indentation radius of a given cantilever tip (AC160TS) was calculated and its response was calibrated by scanning over a reference surface of a known elastic modulus – Polystyrene (PS) surface spin coated on the silicon surface, using the following procedure:

- Solution of 3% wt PS 280kDa (Sigma Aldrich) in toluene was prepared.
- A silicon surface (1x1cm) was plasma cleaned for 30 min.
- The Si surface was covered with the PS solution and spun at 2000 rpm for 60 s.
- The surface was dried well in a desiccator.

Using the AM-FM panel in AsylumResearch program (version 16.10.211) the elasticity output of the AM-FM scan of the PS surface was combined with an elasticity layer based on Hertz Punch model and Silicon <100> tip. The tip radius within the model was adjusted until the elasticity output of the PS surface gave a theoretical value of 3 GPa.[1] This was achieved with the radius of 1.65 nm, as shown in the image below.

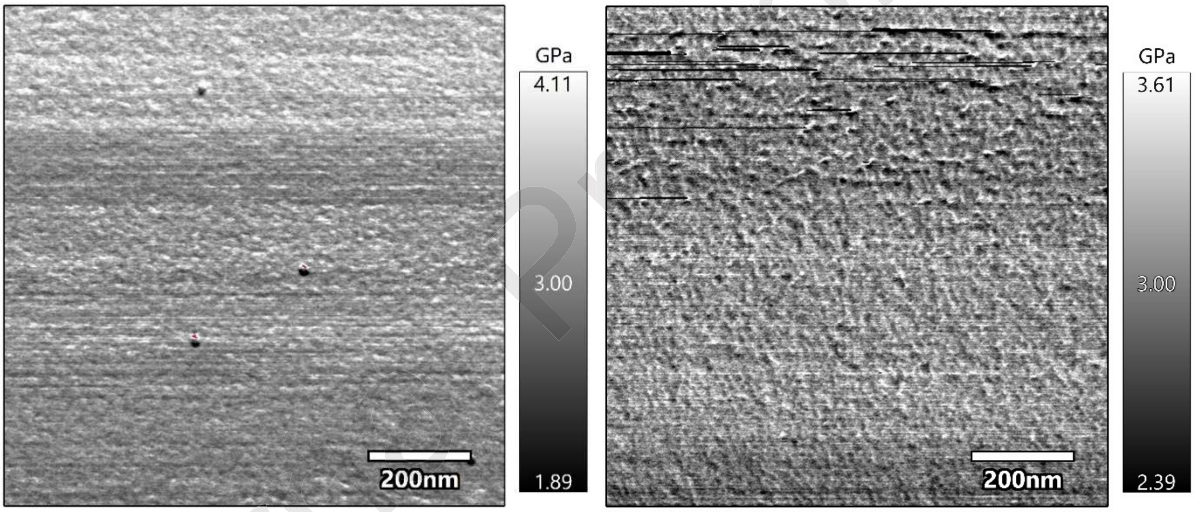

Figure S8. AFM scans of the PS surface with an elasticity layer with R = 1.65 nm such that E ≈ 3 GPa, before (left) and after (right) measuring the LB films. The lack of significant changes between the two calibration experiments implies that the shape of the cantilever tip did not change during the measurement.

An elasticity model with the same tip radius was applied to all AM-FM scans of $Au_{38}(SC_2H_4Ph)_{24}$ films to obtain quantitative nanomechanical data. It was ensured that the exact same cantilever was used for the calibration and the sample measurements and that the shape of the tip did not change considerably during the measurements (for example by being damaged with the sample interaction). Whenever a significant mechanical response took place when scanning an image (for example after passing over a high aggregate), it was assumed that the change was due to tip damage and the calibration and sample measurement were repeated. Furthermore, it was ensured that all the AM-FM parameters were kept as similar as possible between the calibration and different samples. When using the AC160TS cantilever, the free oscillation amplitude of the first mode was kept around 30 nm, the phase around 70 deg and the amplitude of the second mode around 0.3 nm. The free resonant frequencies of the first (f_{01}) and second (f_{02}) mode was 309 kHz and 1.75 MHz respectively.

The tip radius of 1.65 nm calculated from the elasticity model (Hertz Punch) was compared to the shape of the same tip reconstructed from a scan of a perfectly spherical particle (procedure below).

Cantilever tip reconstruction

The cantilever tip shape was reconstructed using an erosion algorithm by Villarubia.[2] This method consists in imaging a known geometry (spherical nanoparticles) with the cantilever to be analyzed. Subsequently, an erosion algorithm is performed using as input the obtained experimental image and the theoretical image of the sphere. The diameter of the nanosphere is inferred from the height of the AFM topography.

The surface with adsorbed nanoparticle was prepared as following: freshly cleaved mica was exposed to 300 ppm Poly(diallyldimethylammonium chloride) (PDADMAC) of molecular weight 400–500 kg/mol purchased from Sigma-Aldrich (Steinman, Germany) for 10 - 20 minutes, water rinsed and nitrogen dried. The surface was exposed to a 100 ppm solution of sulfate latex particles (Invitrogen, Eugene, OR, USA) with diameters of around 20 nm for 10 minutes, gently rinsed with water and nitrogen dried.

The nanoparticle surface was imaged with the cantilever whose tip shape had to be determined. Image of a single isolated particle is shown in Fig. S9a). From the height, the theoretical particle image is calculated and shown in Fig. 9b). The tip shape obtained from the erosion algorithm is shown in Fig. 9c). The red mask in Fig. 9c represents the part of the tip indenting on the surface as obtained from AM-FM AFM.

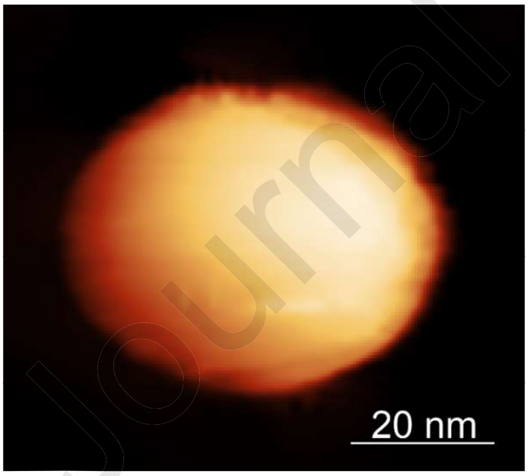

Figure S9a. Particle AFM scan.

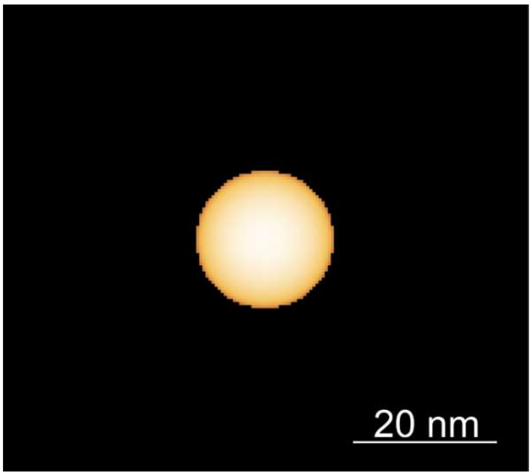

Figure S9b. Calculated theoretical image of the particle.

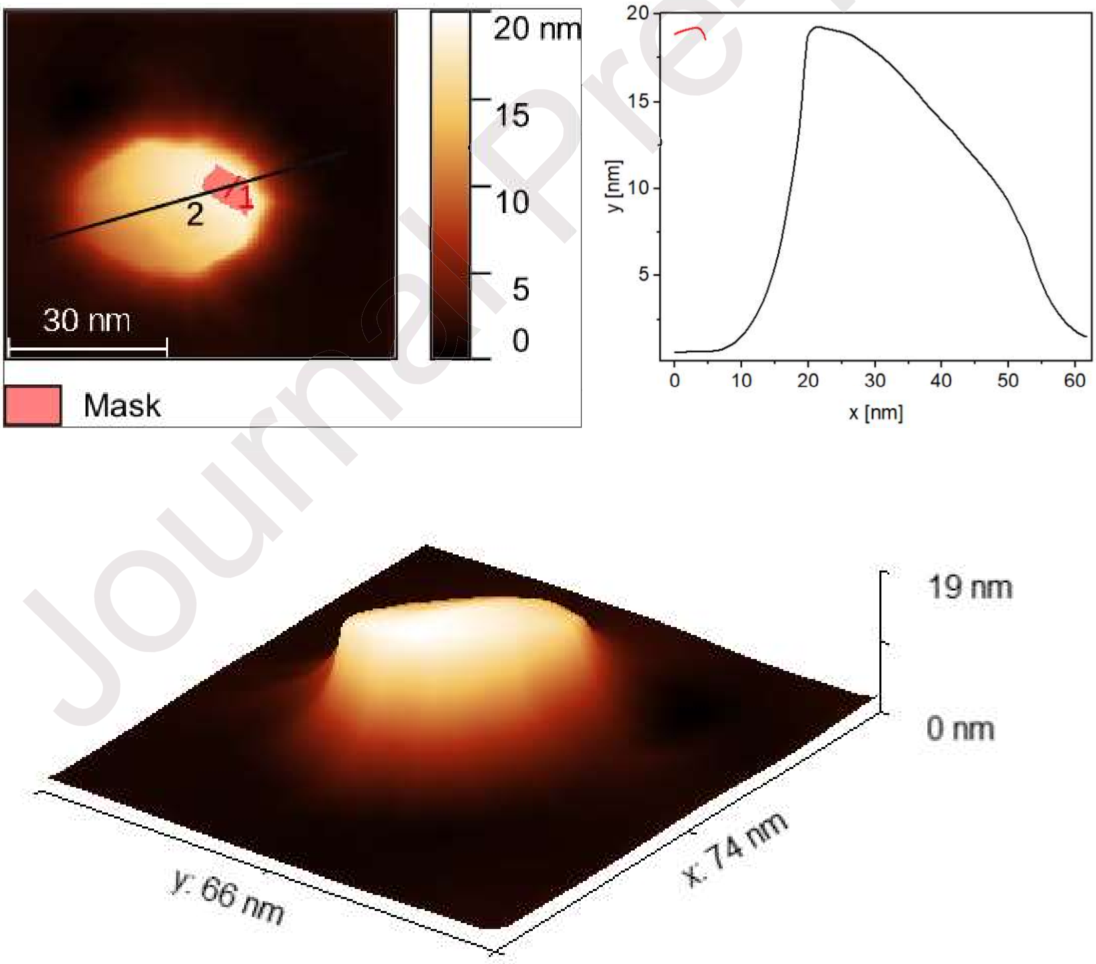

Figure S9c. Image of the reconstructed tip shape (top left) with the corresponding section view (top right) and a 3D view (bottom).

The overall size of the tip is about 16 nm which is much larger than the value obtained from the tip calibration, but it should be noted that the latter should refer to the part of the tip that indents into and interacts most with the sample. The radius of the part of the tip indenting on the surface in AM-FM (shown in red) is about 2 nm which is much closer to the value calculated from the AM-FM cantilever calibration.

1. Moskalyuk, O. A.; Belashov, A. V.; Beltukov, Y. M.; Ivan'kova, E. M.; Popova, E. N.; Semenova, I. V.; Yelokhovsky, V. Y.; Yudin, V. E., Polystyrene-Based Nanocomposites with Different Fillers: Fabrication and Mechanical Properties. *Polymers* **2020,** *12* (11), 2457.
2. Villarrubia, J. S., Algorithms for Scanned Probe Microscope Image Simulation, Surface Reconstruction, and Tip Estimation. *J. Res. Natl. Inst. Stand. Technol.* **1997**, 102, 425-454.

Michal Swierczewski: Investigation, Writing - Original Draft, Visualization. **Alexis Chenneviere:** Investigation. **Lay-Theng Lee:** Conceptualization, Formal analysis, Writing - Review & Editing, Supervision. **Plinio Maroni:** Conceptualization, Investigation, Methodology, Supervision. **Thomas Bürgi:** Conceptualization, Funding acquisition, Writing - Review & Editing, Supervision.

Declaration of interests

☒ The authors declare that they have no known competing financial interests or personal relationships that could have appeared to influence the work reported in this paper.

☐ The authors declare the following financial interests/personal relationships which may be considered as potential competing interests:

Graphical abstract